Electronic Supplementary Information

Real-Time Insight into Nanostructure Evolution during the Rapid Formation of Ultra-Thin Gold Layers on Polymers

Matthias Schwartzkopf,†, Sven-Jannik Wöhnert†, Vivian Waclawek†, Niko Carstens‡, André Rothkirch†, Jan Rubeck†, Marc Gensch†,§, Jonas Drewes‡, Oleksandr Polonskyi‡, Thomas Strunskus‡, Alexander M. Hinz, Simon J. Schaper§, Volker Körstgens§, Peter Müller-Buschbaum§,%, Franz Faupel‡ and Stephan V. Roth†,#*

† Photon Science, Deutsches Elektronen-Synchrotron (DESY), Notkestr. 85, D-22607 Hamburg, Germany

‡ Lehrstuhl für Materialverbunde, Institut für Materialwissenschaft, Christian Albrechts-Universität zu Kiel, Kaiserstr.2, D-24143 Kiel, Germany

§ Lehrstuhl für Funktionelle Materialien, Physik-Department, Technische Universität München, James-Franck-Str. 1, D-85748 Garching, Germany

KTH Royal Institute of Technology, Department of Fibre and Polymer Technology, Teknikringen 56-58, SE-100 44 Stockholm, Sweden

% Heinz Maier-Leibniz Zentrum (MLZ), Technische Universität München, Lichtenbergstraße. 1, D-85748 Garching, Germany

*Corresponding author: Dr. Matthias Schwartzkopf

Mailing address: Deutsches Elektronen-Synchrotron (DESY), Notkestr. 85, D-22607 Hamburg, Germany

Telephone number: +4940/8998-3768

E-mail: matthias.schwartzkopf@desy.de

KEYWORDS

real-time monitoring, nanocluster growth; polymer-metal-interfaces; sputter deposition; grazing incidence, X-ray scattering, ultra-thin films

Present Address

Dr. Oleksandr Polonskyi:

Dept. of Chemical Engineering
University of California, Santa Barbara
Santa Barbara, CA 93106-5080
Mobile: (805) 450-6549

Dr. Alexander M. Hinz:

Fraunhofer Institut für Organische Elektronik, Elektronenstrahl- und Plasmatechnik FEP
Winterbergstraße 28
01277 Dresden, Germany
Email: alexander.martin.hinz@fep.fraunhofer.de

Author Contributions

For this experiment at large scale facility the authors Matthias Schwartzkopf, Sven-Jannik Wöhnert, Niko Carstens, Jan Rubeck, André Rothkirch, Marc Gensch, Jonas Drews, Oleksandr Polonskyi, Thomas Strunskus, Simon J. Schaper, and Volker Körstgens contributed to the alignment of X-ray optics, set up of the sputter chamber at the beamline and performed the *in situ* GISAXS measurements. Alexander M. Hinz designed the sputter chamber and participated in preliminary experiments. Matthias Schwartzkopf analyzed the data, performed IsGISAXS simulations and created all figures. The preparation of polymer templates and static Au/PS/Si samples including AFM measurements were performed by Vivian Waclawek. Stephan V. Roth, Franz Faupel and Peter Müller-Buschbaum provided materials and supervision and participated in the interpretation of the data. The manuscript was written with contributions of all authors and all have given approval to the final version of the manuscript.

Sample preparation

A dedicated mobile DC sputter deposition chamber was integrated in the GISAXS setup at the P03/MiNaXS beamline of the PETRA III synchrotron source at DESY (Hamburg, Germany) to enable *in situ* and real-time observations of the morphological evolution during sputter deposition.[1,2] Sputter deposition was performed using a 50.8 mm in diameter Au target (99.999% purity, Kurt J. Lesker, USA) at an argon working pressure of 0.52×10^{-2} mbar and a discharge power of $P = 100$ W. The resulting effective Au deposition rate of $J = (1.52 \pm 0.07)$ nm/s was determined by a quartz crystal micro balance (QCM, Inficon, Switzerland) positioned above the sample prior deposition. The gold sputter deposition was performed onto $d_{PS} = (88 \pm 2)$ nm thin atactic polystyrene films ($M_w = 270$ kg/mol, Polymer Source Inc., Canada) with a narrow polydispersity ($M_w/M_n = 1.04$) obtained by spin coating for 30 s at a speed of 1800 rpm (Delta 10 TT, SÜSS MicroTec Lithography GmbH, Germany) from 12 g/L polymer solution in toluene (Carl Roth GmbH, Germany) on 12×15 mm² sized Si substrates (Si-Mat, Germany) resulting in a high degree of correlated roughness.[3] According to the supplier, the PS was synthesized by

living anionic polymerization of styrene in THF at -78°C. The molecular weight and polydispersity index (PDI) were obtained by size exclusion chromatography (SEC) in THF. SEC analysis was performed on a Varian liquid chromatograph equipped with refractive and UV light scattering detectors. Note that the samples are not annealed after spin-coating and transferred as-spun to the vacuum chamber for sputter deposition. Prior to spin coating, the Si-wafer pieces were cleaned in an ultrasonic bath filled with acetone for 15 minutes and further rinsed with acetone, isopropanol and ultra-clean water, in order to remove organic residuals. Subsequently, these silicon substrates were oxidized in an acid bath (200 mL of 96% sulfuric acid, 88 mL of 35% hydrogen peroxide (Carl Roth GmbH) and 37.5 mL of deionized water) at a temperature of 80 °C for 15 min. Finally, the cleaned substrates were rinsed with ultra-clean water (18.2 $M\Omega cm^{-1}$) several times and dried in a nitrogen flow.

Grazing-incidence small-angle X-ray scattering

For the sub-millisecond grazing-incidence small-angle X-ray scattering (GISAXS) experiments, an incident beam of photon energy of 13.3 keV was focused to a size of $(25 \times 20)\ \mu m^2$ at the sample position using beryllium compound reflective lenses (Be-CRL).[1,2] The sample-to-detector distance was set to $SDD = (2347 \pm 5)$ mm. A LAMBDA 750K detector system (X-Spectrum GmbH, Germany) based on 2 rows of 6 Si-based Medipix sensors resulting in an array of 1536 by 516 pixel with a pixel size of $(55 \times 55)\ \mu m^2$ was used as X-ray pixel detector.[4] This configuration enabled a high angular resolution of $(0.0013 \pm 0.0002)°$ per pixel combined with a high temporal resolution of 2,000 frames per second (fps) in a continuous-read-write mode respectively a 0.5 ms exposure time. In order to achieve a good separation between the polystyrene (PS), silicon (Si) and gold (Au) Yoneda peaks, an incident angle of $\alpha_i = (0.390 \pm 0.002)°$ was selected during the *in situ* experiments. The X-ray fast shutter and the QCM sample shutter were pneumatically actuated with opening and closing times around 50 ms. All shutters, detector acquisition and the experiment time of $t = 3$ s were controlled by a Python-based script in combination with a programmable logic controller to maximize reproducibility.

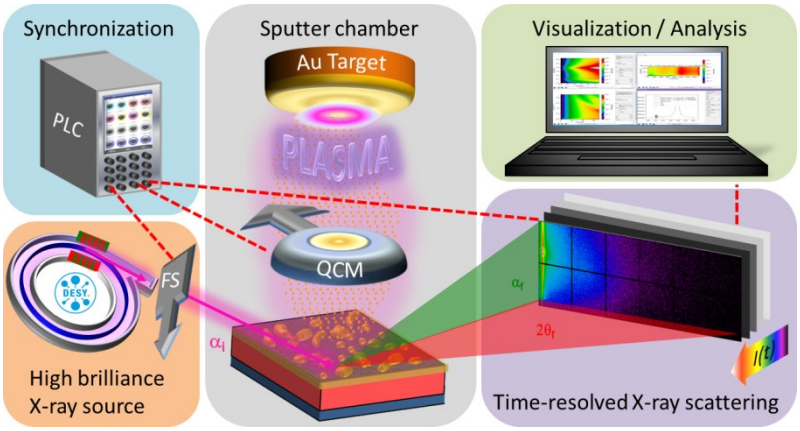

Figure S1: Real-time surface sensitive X-ray scattering measurements: From a programmable logic controller (PLC), trigger signals (red dashed lines) are sent to the X-ray fast shutter (FS), the sample shutter including a quartz microbalance for rate determination (QCM) inside the sputter chamber and the high-speed X-ray detector initiating a synchronized exposure of 6,000 images during 3 seconds of high-rate sputter deposition from a gold target. The time-resolved 2D

X-ray scattering patterns *I(t)* measured under grazing-incidence synchrotron X-ray irradiation ($\alpha_i < 0.4°$) feature the temporal evolution of electron density correlations parallel (along α_f) and perpendicular (along $2\theta_f$) averaged over all non-equilibrium morphologies, which are transferred to a computer for visualization, analysis and simulation-based geometrical modelling *via* a directly programmable data analysis kit.

In total 6,010 frames were recorded, from which 5,175 frames were showing the rapid nanostructure evolution directly after the QCM sample shutter was electronically triggered to move out of the scattering plane indicating the start of sputter deposition. The obtained sub-millisecond GISAXS data sequence was analyzed using the DPDAK software package (SI Fig. S6).[5] A pixel mask was applied to exclude intensity from faulty pixels. The non-equilibrium cluster growth morphology was modeled with geometrical assumptions of a local monodispersed hexagonal arrangement of Au hemispheres.[6] Interpretation of experimental data was supported by simulating sequences of GISAXS scattering patterns within the same setup parameters using IsGISAXS software in a batch processing mode (SI Fig. S10).[7]

Atomic force microscopy

For the measurements of the thin films topography and roughness, an atomic force microscope (AFM) type Solver Next from NT-MDT (Zelenograd, Russia) was used to investigate an interface area of 500 × 500 nm² with a lateral resolution of approx. 0.5 nm. Cantilevers of the type HA_NC "ETALON" (NT-MDT, Zelenograd, Russia) with a resonance frequency f_r (140 ± 14) kHz and a spring constant of k = (3.5 ± 0.7) N/m were used in tapping mode for the measurements at ambient conditions. The probe tip made of silicon was conical tapered at an angle of 30° on the last 200 nm and had a radius of curvature of less than 10 nm. The initial PS film thickness was measured by scanning across a scratch into the polymer thin film using a sharp PTFE tweezer tip (SI Fig. S10).

X-ray thin film interference

Spin-cast polystyrene (PS) thin films on silicon (Si/SiO_x) substrates feature a high degree of correlated interfacial roughness causing strong X-ray thin film interferences (XTFI) related to a constructive interference of X-rays in between the interfaces.[3,8] Whenever monochromatic X-rays irradiate on the PS/air interface under an incident angle α_i, a part of light will be specular reflected, whereas the other light will be either refracted respectively transmitted and/or reflected by the subjacent SiO_x/PS interface depending on the differences in refractive index n at each interface. This second reflection and refraction event will now constructively or destructively interfere with the first reflected light resulting in a characteristic response depending on the thickness and refractive indices of the traversed effective media. These so-called X-ray thin film interferences (XTFI) cause a certain visible oscillations governed by the relation between wavelength of incident light λ and film thickness d_{PS} regarding the light path differences inside thin films.[9] In case of X-ray radiation as used in the present study, the wavelength is below the order of atomic sizes and interacts directly with the electrons in the atoms. The refractive index becomes with $n = 1 - \delta + i\beta$ slightly smaller than one in a complex relation, whereas the imaginary part β of the refractive index reflects the attenuation of the external electromagnetic

field by photoabsorption of the material. The dispersive real part δ of the complex index of refraction for X-rays is expressed by

$$\delta = \frac{\lambda^2}{2\pi} r_e \rho \sum_{j=1}^{Z} \frac{Z_j + f_j'(\lambda)}{M_j} \qquad (1)$$

with wavelength λ, electron radius r_e, the mass density ρ and the sum of number of electrons Z plus the wavelength-dependent atomic scattering factors of all involved atoms $f'(\lambda)$ divided by their molecular weight M.[10] Typical values are $10^{-6} < \delta < 10^{-4}$ and the critical angles for total external reflection are small $\alpha_c \approx \sqrt{2\delta}$. Therefore, small-angle X-ray intensity distributions of thin films under grazing-incidence enable to detect material specific interference.

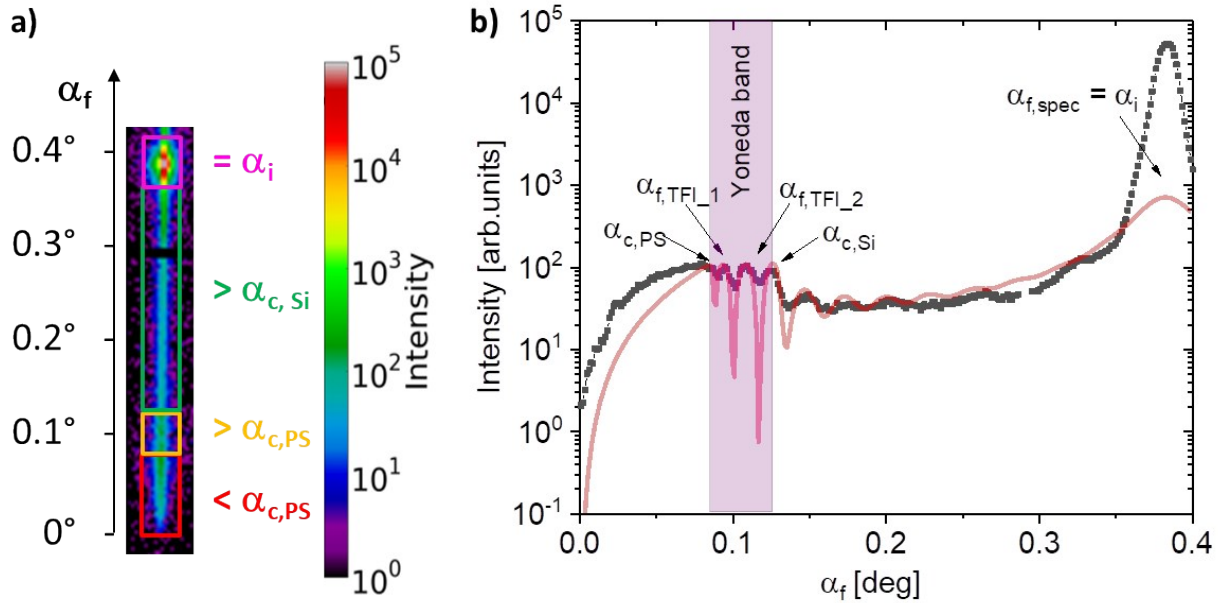

Figure S2: a) Intensity distribution along the reflection plane averaged from -0.0078 nm^{-1} < q_y < 0.0078 nm^{-1} corresponding to 0.1 s exposure time from pristine as-spun PS thin film before high-rate Au sputter deposition depicted as scattering exit angle α_f. The constructive interference of X-ray standing waves between the correlated polymer/air and polymer/silicon interfaces are visible between the critical angle of the polymer thin film $\alpha_{c,PS}$ and the critical angle of silicon $\alpha_{c,Si}$ (Yoneda band) representing key scattering features sensitive to interfacial electron density correlation. **b)** Good agreement to the data of the pristine PS film (black rectangle) was obtained simulating a $\delta_{PS} = 1.326 \times 10^{-6}$ and a film thickness of $d_{PS} = (88 \pm 2)$ nm (red line).

Simulations were performed with IsGISAXS software V2.6 for comparison with the GISAXS data of the morphological parameters deduced from the geometrical growth model in reference. Full 2D scattering patterns with same angular resolution (detector area and pixel size) were calculated based on an input file containing all relevant information about geometry and arrangement of nanoparticles. The calculation of the interference function is based on a regular 1D lattice with a loss of long-range order. The Gaussian disorder parameter ω of the distance D

was set to $\omega = 0.25\ D$. The distorted-wave Born approximation (DWBA) was used to calculate the form factor. The out-of-plane cuts were performed at the same region of interest.

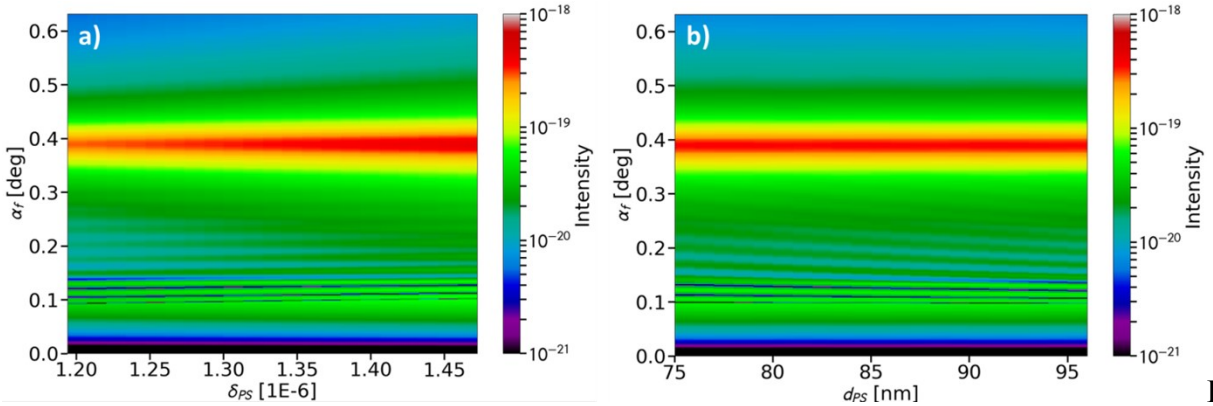

Figure S3: a) Simulated variation of different polymer layer dispersion δ_{PS} at constant $d_{PS} = 88$ nm. **b)** Simulated variation of different polymer layer thickness d_{PS} at constant $\delta_{PS} = 1.3264\times10^{-6}$.

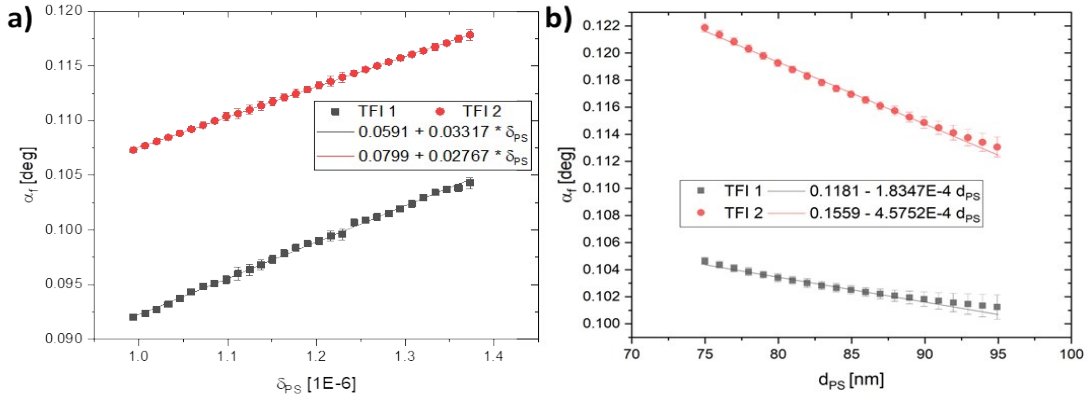

Figure S4: **a)** Simulated variation of δ_{PS} at constant d_{PS} = 88 nm and linear fit to TFI shifts **b)** Simulated variation of d_{PS} at constant $\delta_{PS} = 1.3264\times10^{-6}$ and linear fit to TFI shifts.

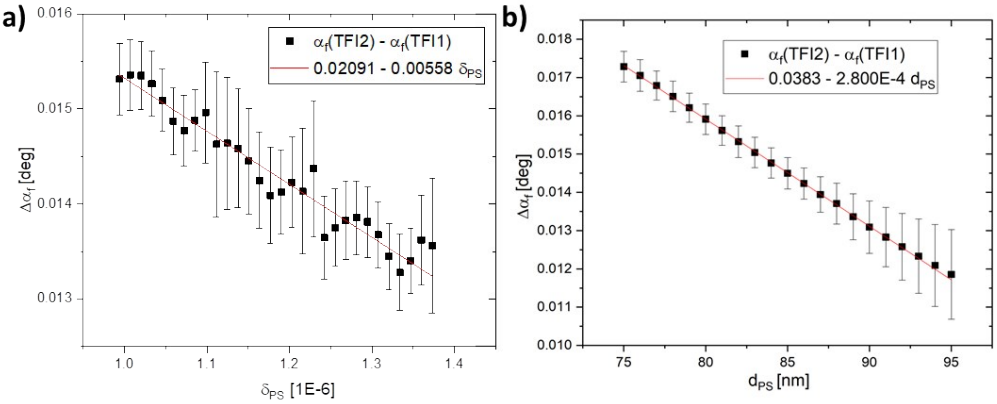

Figure S5: **a)** Difference in α_f of the TFIs as a function of δ_{PS} at constant d_{PS} = 88 nm and linear fit (red). **b)** Difference in α_f of the TFIs as a function of d_{PS} at constant $\delta_{PS} = 1.3264\times10^{-6}$ and linear fit (red).

Automatized data processing in DPDAK[5]

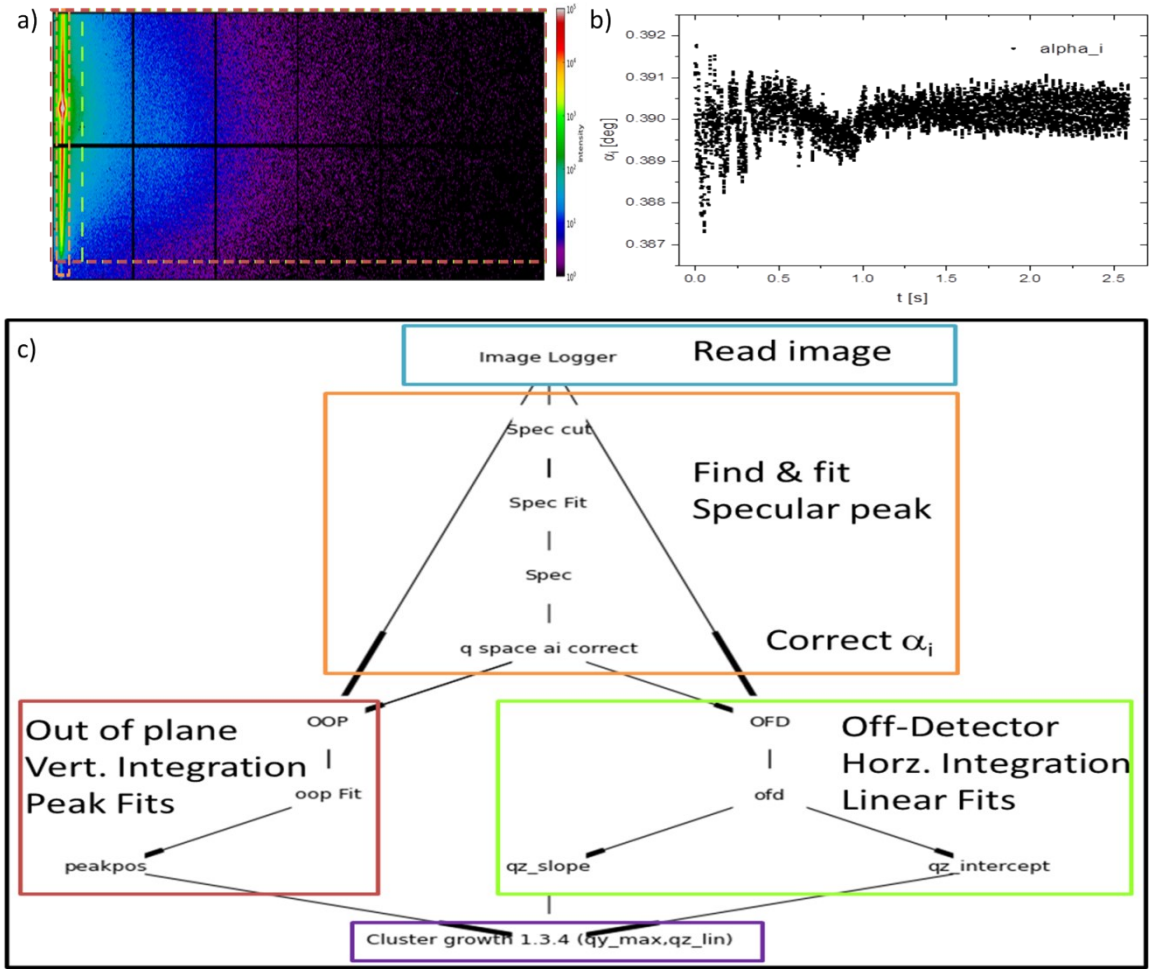

Figure S6: **a)** GISAXS image corresponding to 0.1 s exposure time at the end of high-rate Au sputter deposition around an effective deposited layer thickness of d_{Au} = (3.8 ± 0.1) nm. The dashed rectangular areas are used for integrating intensity: detector cut (orange); out-of-plane cuts (red) and off-detector cuts (green). **b)** evaluated change of incident angle during GISAXS by fitting the specular peak position for correction before integration **c)** DPDAK[5] plugin scheme used for automatized data analysis. After reading the image (blue), the specular peak position was fitted and used to correct incident angle α_i (orange). Subsequently, intensity was vertically (red) and horizontally (green) averaged and the obtained cuts were fitted using Lorentzian and linear regressions, respectively. The parameters were transferred to a customized plugin (cluster growth, violet) directly calculating distances, radii and heights using the hemispherical model[6] and equations from Figure S7.

Sub-Millisecond GISAXS data sequence

The three contour plots in Figure S6 are composed of 5,175 linearly integrated intensity distributions of the obtained GISAXS scattering pattern to visualize evolution of the key scattering features during Au sputter deposition on PS homopolymer thin film. In summary, the different intensity integrations guide to parameterize the relevant key scattering features based on physically motivated equations. These parameterized equations (SI Fig. S7) enable furthermore to describe the changes of average electron densities parallel and perpendicular to the interfaces.

The temporal in plane intensity evolution along the reflection plane as a function of exit angle $I(\alpha_f, t)$ in Figure SI 6a) provides insights in changes of electron density distributions parallel to the surface during the very fast nanostructure formation with a 500 µs time resolution.

At the very beginning of sputter deposition, the specular and the Yoneda peaks become significantly broader and stronger due to a rapid increase of electron density and roughness at the polymer-interface. The position of the specular peak is slightly oscillating due to inherently mechanical induced damped vibration during the fast pneumatic actuated QCM movement, which only becomes significant at sub-millisecond time resolution. The resulting small changes in incident angle of $\Delta\alpha_i \approx \pm 0.02°$ are quantified for each frame and compensated in the further data analysis. Within the first second of Au deposition, a continuous shift of equidistant thin film oscillations to higher exit angles α_f becomes significant in between the Yoneda peaks. This phenomenon can be explained based on the assumption that a fraction of incoming Au atoms are embedded in the PS matrix and the highly mobile adatoms diffuse inside forming a subsurface AuPS enrichment layer. The temporal evolution of the TFI_1 and TFI_2 peak positions in between the Yoneda peaks of PS and Si revealed a non-linear shift towards higher scattering angles (SI Fig. 3b). This is consistent with an increase of the dispersive refractive index δ_{PS} of the polymer matrix, which forms a different effective medium directly affecting the propagation and interference of the X-rays in the sub-surface regime. This continuous shift of TFI significantly slows down around 1.25 s corresponding to an effective deposited gold thickness of $d_{Au} \approx (1.9 \pm 0.1)$ nm indicating a critical gold cluster surface coverage has been reached preventing further embedding and sub-surface diffusion of Au atoms in the polymer matrix. Since the available surface free-volume fraction acting as potential diffusion pathways for Au atoms into the polymer matrix become saturated by the growing Au layer, the temporal angular shift in both TFI peaks $\alpha_{f,TFI}(t)$ were described using an equation adapted from Langmuir adsorption isotherms:

$$\alpha_{f,TFI}(t) = \alpha_{f,0} + A\frac{Kt}{1+Kt} \qquad (2),$$

with $\alpha_{f,0}$ the initial TFI peak position from the pristine PS thin film, A an amplitude and K the adsorption coefficient. The both equidistantly recorded TFI shifts differ only in $\alpha_{f,0}$ while $K = (0.95 \pm 0.01)$ and $A = (0.010 \pm 0.001)$ deg/s are constant (SI Fig. S7).

During deposition and growth of the supported nanogranular gold film, the TFI peaks fade more and more on the one hand due to a reduction of the penetration depth of incoming X-rays by the surface metal coating. On the other hand, the amplitude of the X-ray TFI peaks are also reduced, since the coalescing clusters and their coarse aggregates allocated at the near surface regime grow into more complex morphologies.[11]

The intensity distribution across the reflection plane $I(q_y, d_{Au})$ as a function of the corresponding scattering vector q_y and the effective gold layer thickness d_{Au} visualizes the connection between the effective deposited amount of Au and the average lateral cluster morphology in the near surface regime (Fig. 3c). Directly after starting the gold deposition process, a lateral broadening of the peak $q_{y,1}$ at 0 nm^{-1} is recorded (Fig. 3c). The broadening of intensity distribution $\Delta q_{y,1}$ is attributed to simultaneous changes at the interface electron density, roughness and the occurrence of larger structures out of resolution. The evolution of the FWHM of $q_{y,1}$ is thus sensitive to the formation of a widespread near surface enrichment layer AuPS and correlates to the TFI shifts in Fig. 3b. After a deposition of d_{Au} = (0.27 ± 0.01) nm equivalent to a monolayer of Au atoms (defined as twice the covalent Au atom radius r_{Au}) an increase of out-of-plane intensity distribution $q_{y,2}$ with a maximum around 1.6 nm^{-1} is visible. The maximum of scattering intensity in $q_{y,2}$ represents the most-prominent lateral distance in a paracrystalline lattice and is sensitive to the lateral morphology of the gold cluster layer.[12] The specific shift of the peak position $q_{y,2}(d_{Au})$ is well described using a sum of two opposing exponential functions (Fig. 3d and SI). The temporal evolution of the $q_{y,2}$ intensity distribution below 0.27 nm anticipates a slight shift towards larger q_y values, associated with an initial decrease of interparticle distances due to nucleation at the polymers roughness or created defects due to bombardment.[13] The further continuous shift of this pseudo-Bragg peak towards smaller q_y values is associated with an increase of inter-particle distances D during Au clusters coalescence.[14]

In order to further quantify the increase of electron density distribution vertically at the Au/PS interface during sputter deposition, an additional vertical integration of the out-of-plane intensity distribution was performed along the scattering vector q_z from -2.382 $nm^{-1} < q_y < 0.0689$ nm^{-1} (Fig. 3e). Note that, the non-linear shifts of TFI peaks are also clearly visible here and are not superimposed by the specular reflection. The intensity above the critical angle of Au ($q_{z,c,Au}$ = 0.8387 nm^{-1}) ranging from q_c = 0.85 nm^{-1} to 0.95 nm^{-1} (white dashed box) is increasing. The negative normalized slopes in this region are inverse proportional to the average nanoparticle height H. The evolution of the negative normalized slope obtained by linear regression within the white dashed box $\Delta I/\Delta q_z$ normalized to the intensity value at $I(q_c = 0.85\ nm^{-1})$ can be described by an exponential decay plus linear function (Fig 3f).

The temporal shift in TFI toward higher scattering angles is consistent with an increase of the polymer layer´s dispersion $\delta_{PS}(t)$ induced by the deposition process, as seen qualitatively in the simulations (see SI Fig. S2). According to equation 1, the dispersion is proportional to the effective mass density of the layer. Thus, the change in critical angle allows for a quantification of the amount of gold implanted in the macromolecular matrix considering the temporal shift of the exit angle of the first maximum above the critical angle TFI 1 $\alpha_{f,TFI\_1}(t)$ (Fig. 3b). This shift is correlated to the simulation-based relation to $\alpha_f(\delta_{PS})$ (SI Fig. S3). As seen qualitatively in the simulations (SI Fig. S3), the distance between the key TFI peaks $\Delta\alpha_f$ would slightly decrease for an increase in δ_{PS} due to quenching of the TFI towards the Yoneda peak of Si. However, the evolution of $\Delta\alpha_f$ in the recorded data sequence appears to be constant around (0.015 ± 0.001) degree (Fig. 3b). Thus, the decrease in $\Delta\alpha_f$ from increasing filling factor *via* embedding is potentially compensated by a simultaneous decrease in correlated layer thickness d_{PS} due to growth of Au clusters at the Au/PS interface being not correlated with the underlying PS/Si interface. A linear combination $-\Delta\alpha_f(\delta_{PS}(t)) = \Delta\alpha_f(d_{PS})$ of the above mentioned decrease in TFI´s angular difference caused by the increase of PS layer dispersion $\delta_{PS}(t)$ being equal to the TFI´s angular difference caused by the decrease of correlated PS layer thickness (SI Fig. S3) yields

$d_{PS}(t)$ as depicted in Figure 4a. The correlated PS layer thickness is therefore reduced by embedding and sub-surface cluster growth in the order of approx. 3.5 nm within the first second of deposition. We temporally resolve the formation of a correlated AuPS intermixing layer with a density gradient reported previously from post-deposition X-ray reflectivity measurements.[11,15,16] This growing AuPS layer acts as an additional interface affecting the TFI in the Yoneda band and virtually decrease the correlated PS layer thickness. In other words, the atomic Au implantation and sub-surface Au enrichment simultaneously change the conditions for the X-ray TFI and can be monitored in the GISAXS pattern with sub-millisecond time resolution. With ongoing sputter deposition, the increasing Au coverage will impede these embedding phenomena, leading to a more predominant surface cluster growth.

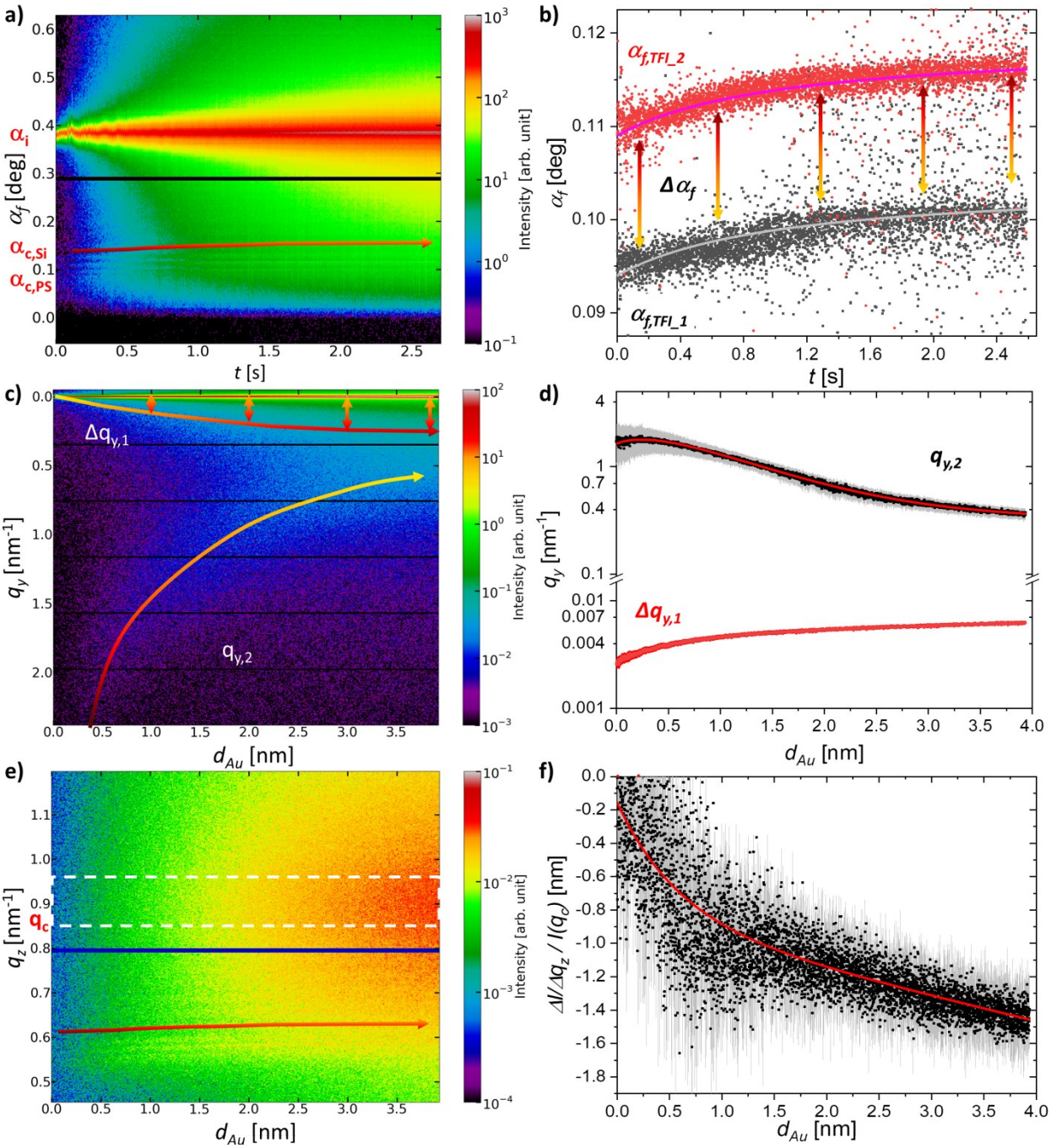

Figure S7: Time-resolved GISAXS data sequence as contour plots and extracted key scattering features: **a)** temporal evolution of the intensity distribution along the reflection plane from -0.0078 nm^{-1} < q_y < 0.0078 nm^{-1} depicted as scattering exit angle α_f. The corresponding key scattering features, incident angle α_i,= 0.3830° critical angle of polystyrene thin film ($\alpha_{c,PS}$) = 0.0831°, silicon substrate ($\alpha_{c,Si}$) = 0.1302°, scale bars are indicated. The colored arrow is a guide to the eye to visualize the shift of thin film interference during high rate sputter deposition. The black horizontal stripes correspond to the insensitive area of the detector. **b)** Extracted peak positions of the both thin film interference (TFI) in the Yoneda band as a function of deposition time. The non-linear increase of the TFI peak positions can be described using an equation

related to Langmuir´s adsorption isotherms (TFI_1: grey line; TFI_2; magenta line). **c)** Evolution of the intensity distribution across the reflection plane depicted as scattering vector q_y from 0.4523 nm^{-1} < q_z < 1.1973 nm^{-1} as a function of effective Au thickness d_{Au}. The colored arrows are guides for the eye to visualize the shifts in peak parameters. The intensity distribution $q_{y,1}$ around the q_y = 0 nm^{-1} broadens from the beginning of sputter deposition. The rise of the out-of-plane intensity distribution $q_{y,2}$ is delayed and shifts continuously towards smaller scattering vectors. **d)** The evolution of the FWHM $\Delta q_{y,1}$ (red spheres) shows a similar behavior as the shifts in TFI in b). The specific shift of the peak position $q_{y,2,max}$ (black rectangles) was fitted using a sum of two opposing exponential functions (red line). **e)** Effective Au thickness d_{Au} evolution of the out-of-plane intensity distribution along the reflection plane from -2.382 nm^{-1} < q_y < 0.0689 nm^{-1} depicted as scattering vector q_z. The non-linear shift of TFI is also visible here (colored arrow). The intensity above the critical angle of Au ($q_{z,c,Au}$ = 0.8387 nm^{-1}) in the range from q_c = 0.85 nm^{-1} to 0.95 nm^{-1} (white dashed box) increase during deposition and is not superimposed by the specular reflection as seen in a). **f)** The evolution of the slope of a linear regression within the white dashed box $\Delta I/\Delta q_z$ normalized to the intensity value at $I(q_c$ = 0.85 nm^{-1}) can be described by an exponential decay plus linear function.

Modeling interface morphology from *in situ* GISAXS data

A simplified general geometrical model was utilized, in order to further extract the average lateral real space parameters of the relatively uncorrelated Au clusters within the X-ray-illuminated volume from the large sequences of *in situ* GISAXS data. The model assumes three equidistantly distributed monodisperse hemispherical clusters composed of the same material volume effectively deposited on the trigonal unit cell surface area in between the clusters.[12] According to size relationships between the model parameters, this analytical approach endorses the extraction and interpretation of tendencies in the nanogranular layer morphology during gold sputter deposition.[2] The model was successfully applied to correlate nanostructure morphology with collective optical and electrical properties of nanogranular silver films during sputter deposition.[17,18] Furthermore, molecular dynamics simulation of Au cluster growth on polymers during sputter deposition independently confirmed the extracted morphological parameters over a wide range.[13]

The evolution of average cluster radii R and distances D as a function of d_{Au} is plotted in Figure 3d and were calculated based on following equation:

$$R(d_{Au}, q_{y,2,max}) = \sqrt[3]{\frac{3^{3/2}}{4\pi} D^2 d_{Au}} \approx \left[3^{3/2} \pi \frac{d_{Au}}{q_{y,2,max}^2} \right]^{1/3} \quad (3).$$

In addition, the evolution of clusters heights was extracted using an IsGISAXS simulation sequence of growing hemispherical clusters in a constant distance on top of a 88nm PS thin film in the framework of the distorted wave Born approximation (DWBA) (SI Fig. S8). We note that this approach empirically endorses the average cluster height determination even for ultra-small clusters in absence of classical key features like height modulations.

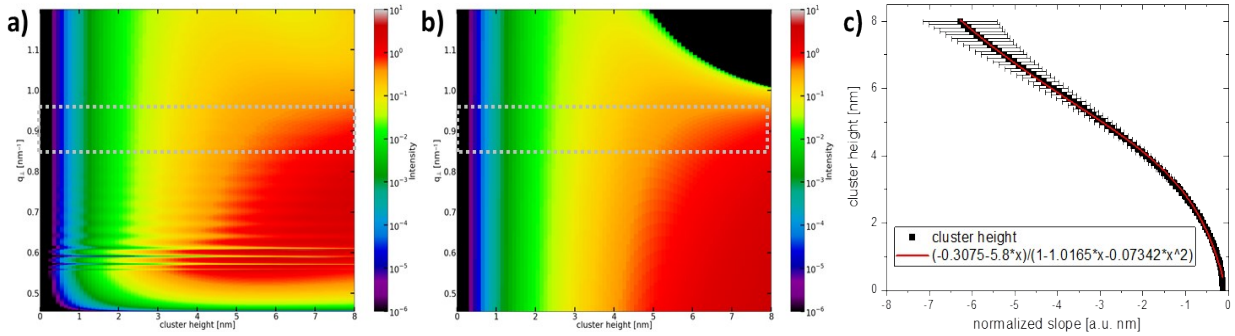

Figure S8: a) Simulated variation of Au hemispherical cluster height on PS from 0.1 nm < H < 8.0 nm. Grey dashed rectangle marks the region 0.85 nm^{-1} < q_{perp} < 0.95 nm^{-1} for the linear fit b) Results of linear fit c) Cluster height as a function of normalized slope (black rectangle) above the critical angle and rational fit (red line) used for height evaluation.

Here, the decrease of slope of a linear regression $I(q) = m \cdot q + n$ along the intensity distribution above the critical angle $\Delta I/\Delta q_z(H)$ is normalized and subsequently parameterized by a fitted rational equation (Fig. S8c). We then connected the relation derived from simulated values to the course of normalized slope $\Delta I/\Delta q_z(d_{Au})/\ I(q_c)$ in the data sequence (Fig. S7f) to extract the evolution of average cluster heights $H(d_{Au})$. The normalized slope for q_c = 0.85 nm^{-1} is calculated by:

$$\Delta I/\Delta q_z/\ I(q_c) = m/(mq_c + n)$$

Uncertainty analysis

The uncertainty analysis is based on Gaussian error propagation of the total differential of the underlying equations considering the individual fitting errors of the key scattering features in the data and simulations as the primary error sources. Thus, for an arbitrary parameter y depending on $(x_n \pm \Delta x_n)$ the error Δy yields:

$$\Delta y = \sqrt{\left(\left|\frac{\partial y}{\partial x_1}\right|\Delta x_1\right)^2 + \left(\left|\frac{\partial y}{\partial x_2}\right|\Delta x_2\right)^2 + \ldots + \left(\left|\frac{\partial y}{\partial x_n}\right|\Delta x_n\right)^2} = \sqrt{\sum_{i=0}^{n}\left(\frac{\partial y}{\partial x_i}\right)^2 {\Delta x_i}^2}$$

Fig. S9 shows the thickness evolution of the fitting errors from the key features in the GISAXS data sequence.

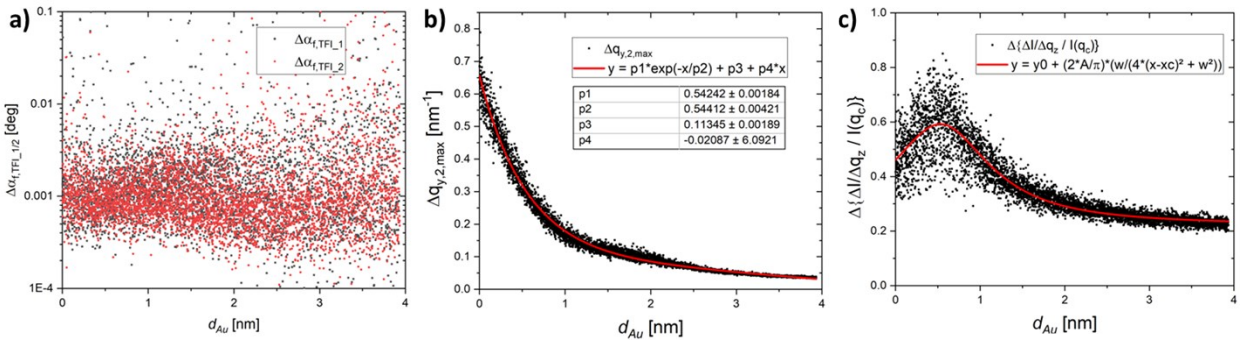

Figure S9: Resulting errors from fitting in the GISAXS sequence of a) the TFI peak positions; b) $q_{y,2,max}$ and c) the normalized slope above the critical angle.

The error of the TFI peak positions scatters around 0.001°. It propagates to an error of the PS layer dispersion $\Delta\delta_{PS} = 0.06\times10^{-6}$, an error of the filling factor $\Delta f_{Au} = 0.2\%$ and an error of the correlated PS layer thickness of $\Delta d_{PS} = 0.65$ nm.

The error of distances ΔD are calculated by

$$\Delta D \approx \frac{2\pi}{q_{y,2,max}^{2}}\Delta q_{y,2,max}$$

The total differential of equation (6) yields for the uncertainty in average radius ΔR:

$$\Delta R \approx \sqrt{\frac{\left(0.8456 q_{y,2,max}\Delta d_{Au}\right)^2 + \left(1.6912\delta\Delta q_{y,2,max}\right)^2}{\sqrt[3]{d_{Au}^{\,2} q_{y,2,max}^{\,5}}^{2}}}$$

with an error of effective Au thickness $\Delta d_{Au} = 0.07$ nm/s = 0.000035 nm/frame.

The error of the cluster height ΔH depends primarily on the fitting error $\Delta\{\Delta I/\Delta q_z/ I(q_c)\}$ of the normalized slope above the critical angle of the cluster material for data and simulation.

$$\Delta\{\Delta I/\Delta q_z/ I(q_c)\} \approx \sqrt{\frac{(n\Delta m)^2 + (m\Delta n)^2}{(m q_c + n)^4}}$$

The evolution of this error is well described using a Lorentzian. Secondarily, ΔH is calculated from the differential of the rational function obtained by parameterizing the simulated decrease of normalized slope proportional to the cluster height (Fig 2):

$$\Delta H\left(\Delta I/\Delta q_z/ I(q_c)\right) \approx \left|\left(-0.3075 * (1.0165 - 2 * 0.07342 * \Delta I/\Delta q_z/ I(q_c)) + 5.8 * (-1 + 0.07342 * \Delta I/\right.\right.$$

The errors for subsequently derived parameters particle density ρ, aspect ratio H/R and number of atoms per cluster N_{Au} are calculated accordingly.

$$\Delta\rho \approx \frac{4 * 10^{14}}{\sqrt{3}D^3}\Delta D$$

$$\Delta(H/R) \approx \sqrt{\left(\frac{\Delta H}{R}\right)^2 + \left(\frac{H\Delta R}{R^2}\right)^2}$$

$$\Delta N_{Au} \approx \frac{0.5}{r^3}\sqrt{(2RH\Delta R)^2 + \left(R^2\Delta H\right)^2}$$

AFM PS thickness measurement

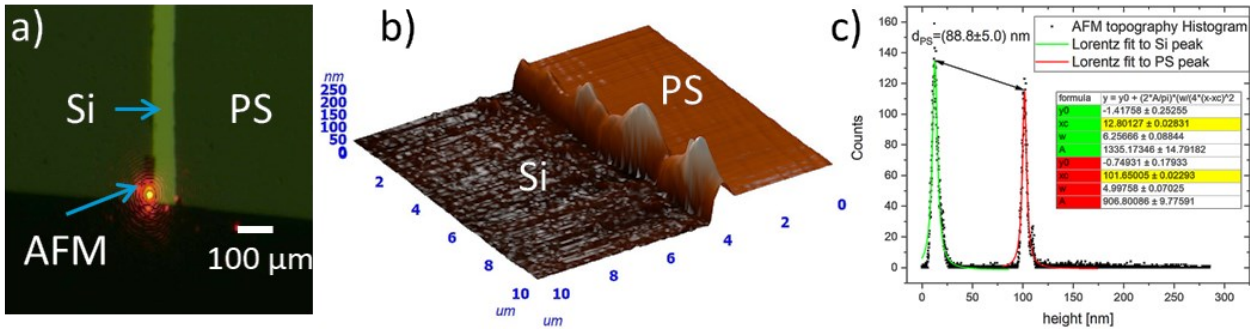

Figure S10: a) microscopic image from the scratched PS/Si sample placed in the AFM; b) 3D AFM topography of the scratch step; c) height histogram with Lorentzian fits to the corresponding Si and PS planes for thickness measurement.

The as-spun PS/Si samples were scratched with sharp PTFE tweezers. The topography of these scratches was measured with AFM subsequently (Fig S10). The raw data is flattened referring to the area of the PS thin film and a histogram is generated to determine the number of elevation points. The two peaks, related to the average height of the silicon substrate and the PS thin film, were each fitted with a Lorentzian function. The corresponding fit parameters are shown in the image. The film thickness is the difference in peak positions and uncertainty is given by the FWHM. Due to the strong radial shear forces and fast solvent removal during spin coating, macromolecules are compressed towards the substrate interface.[19] The R_g of the here used polystyrene (M_w = 270kDa) corresponds to approx. 13 nm.[20] Thus, the vertical profile of the macromolecular network of the as-spun Si/SiO_x/PS (88 nm) substrate basically consists of 6-7 randomly distributed entangled polymer chains replicating the roughness of the native SiO_x layer.[3,21]

Specular Reflectance Spectroscopy

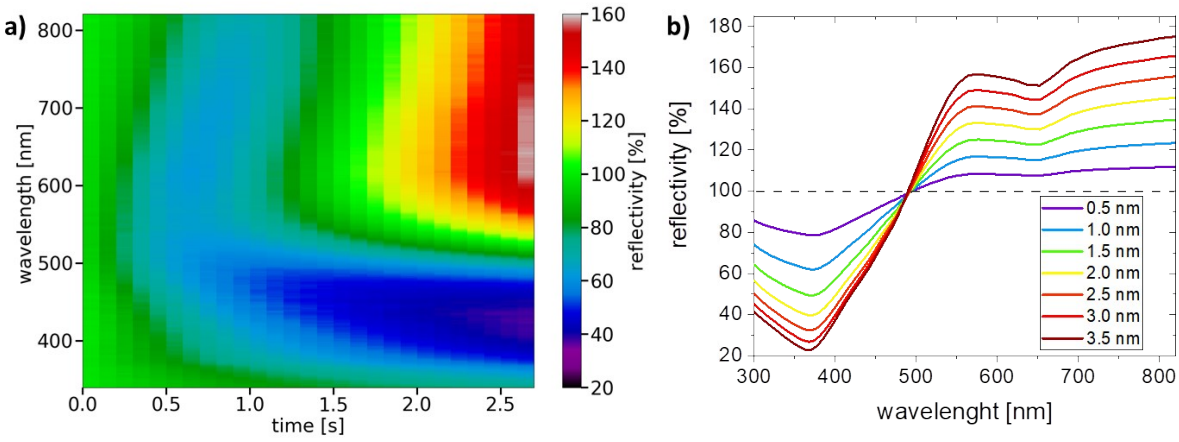

Figure S11: **a)** Normalized *in situ* reflection UV-Vis spectra recorded with an integration time of 100 ms during the first 2.7 seconds of gold sputter deposition at a rate of 1.5nm/s; **b)** Simulated reflectivity spectra using Reflectance Calculator from Filmetrics of Au/PS/Si at different Au bulk layer thicknesses normalized to simulated PS(90nm) on Si-wafer.

The *in situ* reflection UV-Vis measurements were carried out by illuminating an area of approximately 30 mm^2 in the center of the sample surface with a deuterium halogen light source (Ocean Optics, DH-2000-BAL) and recording the reflected signal during Au sputter deposition by means of a spectrometer (Ocean Optics, STS-VIS) covering the range from 350 nm to 800 nm. The light source, spectrometer and corresponding lens system (Thor Labs) were installed at an angle of 55° with respect to the sample surface at chamber viewports. The viewports are made of fused silica to ensure no signal loss at the windows. Before the start of the measurements, a reference reflection spectrum of the bare PS/Si substrate was taken. All measured spectra were normalized to this reference where the reflection intensity of the bare substrate was set to a level of 100%. The sputter process was performed at a power of 100 W, an argon flow of 10 sccm and an operating pressure of 5.4×10^{-3} mbar. The recording of *in situ* UV-Vis spectra started after a sufficient period of pre-sputtering where the sample was protected by a shutter system until stable deposition conditions were ensured (as monitored by QCM). Reflection spectra were recorded during the first 2.7 seconds of gold film growth with an integration time of 100 ms. The spectra were not averaged or smoothed (Figure S11 a). Interpretation of experimental data was supported by calculating different reflectance spectra solely due to thin-film interference in the UV/Vis/NIR range from 200 nm to 1000 nm using Reflectance Calculator from Filmetrics based on the complex-matrix form of the Fresnel equations (Figure S11 b).

Abbreviations

GISAXS, grazing-incidence small-angle X-ray scattering; PS, polystyrene; XTFI, thin film interference; MD, molecular dynamics simulations; DFT, density functional theory; TEM, transmission electron microscopy; rms, root-mean-square; LAMBDA, large area medipix3-based detector array; DC, direct current; FWHM, full width at half maximum; QCM, quartz crystal microbalance; DWBA, distorted wave Born approximation.

References

1 A. Buffet, A. Rothkirch, R. Döhrmann, V. Körstgens, M. M. Abul Kashem, J. Perlich, G. Herzog, M. Schwartzkopf, R. Gehrke, P. Müller-Buschbaum and S. V Roth, *J. Synchrotron Radiat.*, 2012, **19**, 647–53.

2 M. Schwartzkopf, A. Hinz, O. Polonskyi, T. Strunskus, F. C. Löhrer, V. Körstgens, P. Müller-Buschbaum, F. Faupel and S. V Roth, *ACS Appl. Mater. Interfaces*, 2017, **9**, 5629–5637.

3 P. Müller-Buschbaum and M. Stamm, *Macromolecules*, 1998, **31**, 3686–3692.

4 D. Pennicard, S. Lange, S. Smoljanin, H. Hirsemann and H. Graafsma, *J. Instrum.*, , DOI:10.1088/1748-0221/7/11/C11009.

5 G. Benecke, W. Wagermaier, C. Li, M. Schwartzkopf, G. Flucke, R. Hoerth, I. Zizak, M. Burghammer, E. Metwalli, P. Müller-Buschbaum, M. Trebbin, S. Förster, O. Paris, S. V. Roth and P. Fratzl, *J. Appl. Crystallogr.*, 2014, **47**, 1797–1803.

6 M. Schwartzkopf, A. Buffet, V. Körstgens, E. Metwalli, K. Schlage, G. Benecke, J. Perlich, M. Rawolle, A. Rothkirch, B. Heidmann, G. Herzog, P. Müller-Buschbaum, R. Röhlsberger, R. Gehrke, N. Stribeck and S. V Roth, *Nanoscale*, 2013, **5**, 5053–62.

7 R. Lazzari, *J. Appl. Crystallogr.*, 2002, **35**, 406–421.

8 B. Lin, T. L. Morkved, M. Meron, Z. Huang, P. J. Viccaro, H. M. Jaeger, S. M. Williams and M. L. Schlossman, *J. Appl. Phys.*, 1999, **85**, 3180.

9 S. Kinoshita and S. Yoshioka, 2005, 1442–1459.

10 B. Henke, E. Gullikson and J. Davis, *At. data Nucl. data tables*, 1993, **54**, 181–342.

11 M. Schwartzkopf, G. Santoro, C. J. Brett, A. Rothkirch, O. Polonskyi, A. Hinz, E. Metwalli, Y. Yao, T. Strunskus, F. Faupel, P. Müller-Buschbaum and S. V. Roth, *ACS Appl. Mater. Interfaces*, 2015, **7**, 13547–13556.

12 M. Schwartzkopf, A. Buffet, V. Körstgens, E. Metwalli, K. Schlage, G. Benecke, J. Perlich, M. Rawolle, A. Rothkirch, B. Heidmann, G. Herzog, P. Müller-Buschbaum, R. Röhlsberger, R. Gehrke, N. Stribeck and S. V Roth, *Nanoscale*, 2013, **5**, 5053–62.

13 J. W. Abraham, T. Strunskus, F. Faupel and M. Bonitz, *J. Appl. Phys.*, 2016, **185301**, 1–12.

14 R. Hosemann and S. N. Bagchi, *Acta Crystallogr.*, 1952, **5**, 612–614.

15 G. Kaune, M. A. Ruderer, E. Metwalli, W. Wang, S. Couet, K. Schlage, R. Röhlsberger, S. V. Roth and P. Müller-Buschbaum, *ACS Appl. Mater. Interfaces*, 2009, **1**, 353–360.

16 S. Yu, G. Santoro, Y. Yao, D. Babonneau, M. Schwartzkopf, P. Zhang, S. K. Vayalil, P. Wessels, R. Döhrmann, M. Drescher, P. Müller-Buschbaum and S. V Roth, *J. Phys. Chem. C*, 2015, **119**, 4406–4413.

17 G. Santoro, S. Yu, M. Schwartzkopf, P. Zhang, S. Koyiloth Vayalil, J. F. H. Risch, M. A. Rübhausen, M. Hernández, C. Domingo and S. V. Roth, *Appl. Phys. Lett.*, 2014, **104**, 243107.

18 M. Gensch, M. Schwartzkopf, W. Ohm, C. J. Brett, P. Pandit, S. K. Vayalil, L. Bießmann, L. P. Kreuzer, J. Drewes, O. Polonskyi, T. Strunskus, F. Faupel, A. Stierle, P. Mu and S. V Roth, *ACS Appl. Mater. Interfaces*, 2019, **11**, 29416–29426.

19 D. W. Schubert and T. Dunkel, *Mater. Res. Innov.*, 2003, **7**, 314–321.

20 K. Terao and J. W. Mays, *Eur. Polym. J.*, 2004, **40**, 1623–1627.

21 F. Faupel, R. Willecke and A. Thran, *Mater. Sci. Eng. R Reports*, 1998, **22**, 1–55.